

# Taming the nucleation and growth kinetics of lead halide perovskite quantum dots

**Maksym Kovalenko** (✉ [mvkovalenko@ethz.ch](mailto:mvkovalenko@ethz.ch))

Swiss Federal Institute of Technology in Zurich <https://orcid.org/0000-0002-6396-8938>

**Quinten Akkerman**

ETH Zurich

**Tan Nguyen**

University Rennes

**Simon Boehme**

ETH Zurich <https://orcid.org/0000-0002-8399-5773>

**Federico Montanarella**

ETH Zurich

**Dmitry Dirin**

ETH Zurich

**Philipp Wechsler**

ETH Zurich

**Finn Beiglböck**

ETH Zurich

**Rolf Erni**

Swiss Federal Laboratories for Materials Science and Technology <https://orcid.org/0000-0003-2391-5943>

**Claudine Katan**

Univ Rennes, CNRS, <https://orcid.org/0000-0002-2017-5823>

**Jacky Even**

Institut FOTON UMR CNRS 6082 <https://orcid.org/0000-0002-4607-3390>

---

**Physical Sciences - Article**

**Keywords:**

**Posted Date:** February 25th, 2022

**DOI:** <https://doi.org/10.21203/rs.3.rs-1236393/v1>

**License:**  This work is licensed under a Creative Commons Attribution 4.0 International License.

[Read Full License](#)



# **Taming the nucleation and growth kinetics of lead halide perovskite quantum dots**

*Quinten A. Akkerman,<sup>1,2,\*</sup> Tan P. T. Nguyen,<sup>3</sup> Simon C. Boehme,<sup>1,2</sup> Federico Montanarella,<sup>1,2</sup> Dmitry N. Dirin,<sup>1,2</sup> Philipp Wechsler,<sup>1</sup> Finn Beiglböck,<sup>2</sup> Rolf Erni,<sup>4</sup> Claudine Katan,<sup>3</sup> Jacky Even<sup>5</sup> and Maksym V. Kovalenko<sup>1,2</sup>*

<sup>1</sup>Department of Chemistry and Applied Biosciences, ETH Zürich, Zürich CH-8093, Switzerland

<sup>2</sup>Empa-Swiss Federal Laboratories for Materials Science and Technology, Dübendorf, CH-8600, Switzerland

<sup>3</sup>Univ Rennes, ENSCR, INSA Rennes, CNRS, ISCR - UMR 6226, F-35000 Rennes, France

<sup>4</sup>Electron Microscopy Center, Empa – Swiss Federal Laboratories for Materials Science and Technology, Dübendorf, Switzerland.

<sup>5</sup>Univ Rennes, INSA Rennes, CNRS, Institut FOTON - UMR 6082, F-35000 Rennes, France

\*Current address: Lehrstuhl für Photonik und Optoelektronik, Nano-Institut München und Fakultät für Physik, Ludwig-Maximilians-Universität (LMU), Königinstr. 10, D-80539 München, Germany

Correspondence: mvkovalenko@ethz.ch

Colloidal lead halide perovskite (LHP) nanocrystals (NCs)<sup>1-6</sup>, with bright and spectrally narrow photoluminescence (PL) tunable over the entire visible spectral range, are the latest generation of semiconductor quantum dots (QDs) of immense interest as classical and quantum light sources<sup>7-9</sup>. LHP NCs form by sub-second fast and hence hard-to-control ionic metathesis reactions, which severely limits the access to size-uniform and shape-regular NCs in the sub-10 nm range. We posit that a synthesis path comprising an intricate equilibrium between the precursor ( $\text{PbBr}_2$ ) and the  $\text{Cs}[\text{PbBr}_3]$  solute for the QD nucleation may circumvent this challenge. Here, we report a room-temperature synthesis of monodisperse, isolable spheroidal  $\text{CsPbBr}_3$  QDs, size-tunable in the 3-13 nm range. The kinetics of both nucleation and therefrom temporally separated growth are drastically slowed down by the formation of transient  $\text{Cs}[\text{PbBr}_3]$ , resulting in total reaction times of up to 30 minutes. The methodology is then extended to  $\text{FAPbBr}_3$  (FA = formamidinium) and  $\text{MAPbBr}_3$  (MA = methylammonium), allowing for thorough experimental comparison and modelling of their physical properties under intermediate quantum confinement. In particular, QDs of all these compositions exhibit up to four excitonic transitions in their linear absorption spectra and we demonstrate that the size-dependent confinement energy for all transitions is independent of the A-site cation.

Colloidal LHP NCs have recently become popular light-emissive materials<sup>4-6</sup>, of practical interest for LEDs<sup>10-13</sup>, LCD displays<sup>14-16</sup>, lasers<sup>17-20</sup>, scintillators<sup>21,22</sup> and luminescent solar concentrators<sup>23-25</sup>. They are much praised for simultaneously exhibiting near-unity PL quantum yields (QYs), a PL peak tailorabile across the 410-800 nm spectral range with small PL full widths at half maximum (FWHM, <100 meV), large-absorption cross-sections<sup>26</sup>, long exciton coherence times and sub-ns fast radiative rates at low temperatures<sup>27-29</sup>. Much scientific interest revolves around single-photon emission from LHP NCs<sup>7,8,29-31</sup> and collective phenomena in LHP NC assemblies such as superfluorescence<sup>9,32-34</sup>.

Until now, and owing to their synthetic availability, most studies on colloidal LHP NCs focused on relatively large NC sizes, i.e. with diameters of around or exceeding 10 nm. In this weak excitonic confinement regime, tunability of the bandgap energy is predominantly achieved via mixed-halide compositions. Structurally soft, with rather ionic chemical bonding, LHP NCs vastly, rather orthogonally, differ to more conventional QD materials such as CdSe and InP having covalent and rigid crystal structure. One such difference is the difficulty in producing small LHP QDs, down to few nanometers in diameter, thus hindering the studies into the diverse expressions of the strong size-quantization of excitons in LHPs (and practical use thereof) as well as understanding of the mechanism of LHP QD formation. High lattice ionicity and low lattice formation energy of LHP NCs is a mixed blessing when it comes to the synthesis of small QDs: they form too quickly as ionic co-precipitation, with sub-second formation kinetics. In this regard also the surface capping ligands – crucially important for the controlled nucleation and growth as well as for the structural integrity of the resulting QDs and their stability against solvents and environment – bind in a non-covalent and dynamic manner<sup>35</sup>, thus contributing to the difficulty of arresting the QD formation and stabilizing them at small sizes.

Monodispersity and shape-uniformity, as well as precise size-tunability in the sub-10 nm regime must be realized through the scalable synthesis that yields isolable, pure and robust QD samples. Thus far no synthesis method fulfilling the entirety of these requirements has been reported for small LHP QDs. Limited success had been reached for CsPbX<sub>3</sub> (X Cl, Br, I) compositions<sup>34,36,37</sup>, wherein QD fractions down to 3-4 nm are obtained post-synthetically, albeit with small synthesis yield for a specific QD size fraction, foremost due to broad size dispersion or very lossy isolation. Noteworthy is the use of long-chain zwitterionic capping

ligands that exhibit improved surface adhesion relative to more conventional single-binding-head molecules, rendering the small  $\text{CsPbBr}_3$  QDs sufficiently robust to sustain multiple steps of size-selective precipitation leading to monodisperse fractions<sup>34</sup>. Small colloidal  $\text{FAPbX}_3$  and  $\text{MAPbX}_3$  NCs, however, remained elusive as they are even more labile structurally.

We reasoned that the slower formation of small monodisperse LHP QDs at full reaction yield cannot be accomplished only by mere adjustments of typical reaction parameters, such as lowering of the reaction temperature and concentration of reagents. We hypothesized that precursor-monomer-QD nuclei conversion path must be characterized by the mutual chemical equilibrium between these moieties governed by the common complexing agent, thus having a self-limiting character as well. Importantly, this equilibrium shall not be obscured by any competing process, such as binding of a stronger capping ligand to the QD surface, which is somewhat contradictory to the previous efforts on stabilizing the perovskite NC surfaces by stronger binding ligands. We find that trioctylphosphine oxide (TOPO) serves this three-fold mission as it complexes (solubilizes) the  $\text{PbBr}_2$  precursor, binds to the  $\text{Cs}[\text{PbBr}_3]$  monomer (solute) and then weakly coordinates to the QD nuclei surface. The issue of isolation and subsequent robustness of the obtained QDs is then mitigated by adding a stronger binding ligand – lecithin as a long-chain zwitterion – at the end of the QD formation step. We thus present a room-temperature synthesis, wherein the overall QD formation occurs on the scale of up to 30 minutes, hereby allowing also the live *in-situ* observation of the reaction by optical absorption and emission spectroscopy. After the isolation, monodisperse rhombicuboctahedral  $\text{CsPbBr}_3$  QDs, with mean size tunable in 3-13 nm range, are obtained at 100% precursor-to-QD conversion rate. These  $\text{CsPbBr}_3$  QDs, as well as  $\text{FAPbBr}_3$  and  $\text{MAPbBr}_3$  QDs obtained analogously, exhibit up to four well-resolved excitonic transitions and the size-dependent confinement energies for all transitions is independent of the A-site cations. The obtained energies of these transitions, utilizing the statistics from over 25.000 individual spectra, are then found to agree with those calculated using effective mass/ $\mathbf{k}\cdot\mathbf{p}$  model.

### Synthesis of monodisperse $\text{CsPbBr}_3$ QDs.

We sought to tame the nucleation and growth of LHP QDs while ensuring a facile one-pot synthesis methodology that uses off-the-shelf chemicals and that is suited for *in-situ* monitoring with optical and

structural methods, as well as for *ex-situ* characterization (**Fig.1**). We hypothesized that the conventional approach – referred to as oleylamine - oleic acid (OLAM/OA) path<sup>1</sup> – suffers from the immediate conversion of the PbBr<sub>2</sub> into haloplumbate ionic solute (PbBr<sub>3</sub><sup>-</sup>) upon the action of OLAM/OA<sup>38,39</sup>. The subsequent reaction with injected Cs-ions is thus quantitative and fast, and hence nucleation and growth are not temporally separated. We thus aimed at establishing the mechanism, in which the formation of PbBr<sub>3</sub><sup>-</sup> anions is activated to the introduction of Cs-cations by having the latter as the only available cation in the system throughout the synthesis, and wherein the equilibrium is retained with the non-reactive PbBr<sub>2</sub> precursor reservoir through a common coordinating agent. We therefore took an approach of using a neutral molecule TOPO as a sole coordinating agent for solubilizing PbBr<sub>2</sub> precursor<sup>40</sup>. Into this PbBr<sub>2</sub>:TOPO solution, Cesium-diisooctylphosphinate (Cs-DOPA) solution was injected at room temperature (both in hexane; see **Methods, Supplementary Note 1 and Supplementary Figs. 1-5**). Since TOPO and DOPA are weakly binding ligands for LHP QDs<sup>40,41</sup>, they were displaced with lecithin as a strongly binding zwitterionic ligand<sup>42</sup> for subsequent isolation and purification steps, as well as *ex-situ* characterization (see detailed comparison of *in-situ* and *ex-situ* data analysis, as well as the *in-situ* set up in **Extended Data Fig.1, Supplementary Note 1.2 and Supplementary Figs. 6-12**). *In-situ* recorded absorption spectra (**Supplementary Video 1**, 6 nm CsPbBr<sub>3</sub> QDs) exemplify the slow growth lasting for 30 minutes and narrow size-dispersion seen as sharp excitonic absorption peaks. Purified lecithin-coated QDs exhibit the same sharp absorption features when measured *ex-situ* and can be prepared in a size range from 3-13 nm (**Fig.1d and Supplementary Fig. 13**). *In-situ* synchrotron SAXS measurement (6.2 nm QDs, **Fig. 1e**) yielded narrow size-dispersion (8.1%) and rather isotropic spheroidal shape. The latter is in stark contrast to previous *ex-situ* SAXS measurements on cuboidal shaped CsPbBr<sub>3</sub> QDs, where on average a 20% offset between the shortest and longest edge length of the cuboid was reported<sup>34,42</sup>. The findings hold also for 12 nm-large QDs (**Supplementary Fig. 14**). TEM and scanning TEM (STEM) images of purified 8 nm QDs (**Fig. 1f and Supplementary Figs. 15-16**) showing tendency to hexagonal packing, indicating spheroidal QDs, rather than the commonly observed nanocubes.<sup>1,9,34,36,37</sup> High-resolution STEM (HR-STEM) of 12 nm QDs evidences truncation along the {110} and {111} facets, hence rhombicuboctahedral shape of QDs (**Extended Data Fig.2**), in good-agreement with the spheroidal shape in *in-situ* SAXS. CsPbBr<sub>3</sub> QDs crystallize in a phase-pure orthorhombic phase as seen from *in-situ* WAXS of crude solutions as well as

powder X-ray diffraction (XRD, **Fig. 1g**). CsPb(Cl:Br)<sub>3</sub> QDs, which exhibit larger bandgaps compared to CsPbBr<sub>3</sub>, and therefore of interest for blue LEDs, could also be obtained using this method by applying an *in-situ* anion exchange<sup>43,44</sup>, using ZnCl<sub>2</sub>-TOPO solution added dropwise before lecithin ligand. Here, the sharp excitonic features (**Extended Data Fig. 3a and b**) and narrow size-dispersion and spheroidal shape (**Extended Data Fig. 3c, d and Supplementary Fig. 17**), were fully preserved.

*In-situ* optical measurements allow for thorough and fast parametric screening. The overall dilution and the concentration of the TOPO ligands were found most effective for controlling the QD size in our room-temperature synthesis, contrary to conventional size control by varying the reaction temperature<sup>1,34,36,42,45,46</sup>. For instance, dilution of the reaction by an order of magnitude leads to a decrease in size from 9 nm to 3 nm (**Fig. 1h, i and Extended Data Fig. 4a**). Similar effects come from adjusting concentrations of PbBr<sub>2</sub> or Cs-DOPA precursors individually (**Supplementary Note 1.1 and Supplementary Figs. 1-4**). Alternatively, a four-fold raise in TOPO concentration translates in the QD size increase from ca. 3 to 9 nm (**Fig. 1j, k and Extended Data Fig. 4b**). A combined effect of dilution and larger TOPO concentration translates into drastically slower QD growth (**Fig. 1l, Supplementary Fig. 18 and Supplementary Video 2**).

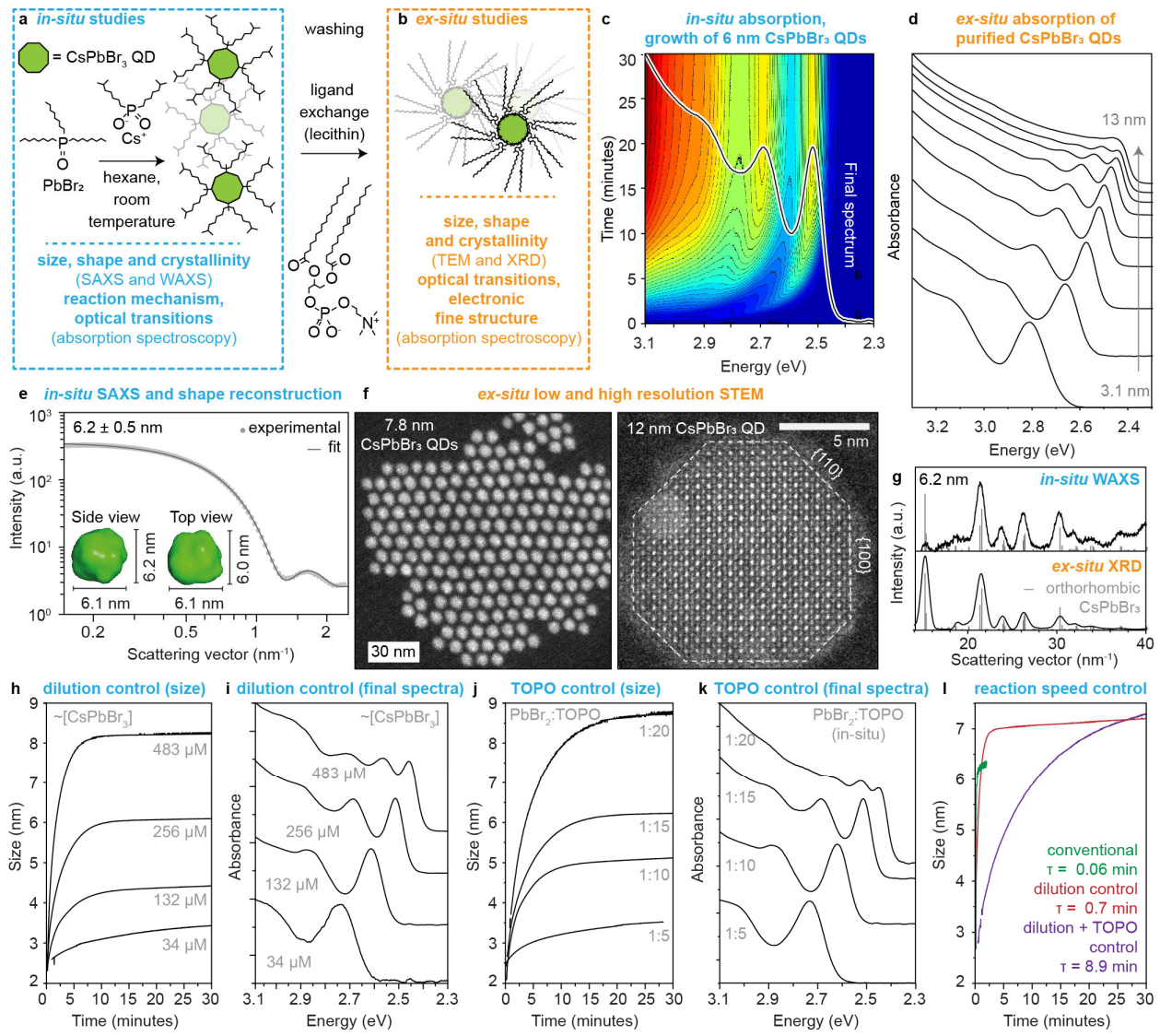


**Fig. 1 | Room-temperature, controlled-rate synthesis of monodisperse  $\text{CsPbBr}_3$  QDs.** **a**, A reaction scheme and overview of *in-situ* monitoring techniques. **b**, Overview of used *ex-situ* techniques on ligand exchanged and washed QDs which are complementary with the used *in-situ* techniques. **c**, Example of *in-situ* recorded absorption spectra of 6 nm QD during 30 min reaction with solid line being the final recorded absorption spectrum, demonstrating clear and sharp first and higher order absorption peaks. **d**, Absorption spectra of series of washed  $\text{CsPbBr}_3$  QDs ranging from roughly 3 to 13 nm. **e**, SAXS scattering curve of 6 nm QD recorded at the end of a reaction, resulting in a size dispersion of roughly 8%, and a fitted pseudo spherical shape with one axis being slightly shorter compared to the other two. **f**, STEM image of washed 7.8 nm QDs and HRSTEM image of a single QD showing the pseudo spherical shape due to truncation. **g**, Diffractograms of 6.2 nm QD recorded both *in-situ* in a crude solution using WAXS as well as from a washed dispersion using XRD on a film, both exhibiting a match with the orthorhombic crystal structure of  $\text{CsPbBr}_3$ . **h**, *In-situ* recorded size of  $\text{CsPbBr}_3$  QDs at various concentrations (concentration of Cs-DOPA) showing both the decrease in size and reaction speed upon dilution. **i**, Respective final absorption spectra of reactions shown in panel h, indicating all final samples are highly monodisperse. **j**, *In-situ* recorded size of  $\text{CsPbBr}_3$  QDs at various  $\text{PbBr}_2:\text{TOPO}$  ratios (with a fixed  $\text{PbBr}_2$  concentration) showing the increase in size with increasing TOPO concentration, whilst the reaction speed remains relatively unchanged. **k**, Respective final absorption spectra of reactions shown in panel c, indicating all final samples are highly monodisperse. **l**, Comparison of reaction speeds of three different reactions resulting in roughly the same QDs size,

showing how controlling both the overall dilution and the TOPO concentration can slow down the reaction by two orders of magnitude.

### Spheroidal vs cuboidal QDs.

Next, we elucidated the origin of the exceptionally well-resolved excitonic transitions in the spheroidal QDs, as compared to conventional cuboidal NCs studied since 2015<sup>1</sup>. The difference cannot be merely attributed to the size-dispersion. For instance, **Fig. 2a and b** compare our spheroidal CsPbBr<sub>3</sub> QDs with several own examples of cuboidal CsPbBr<sub>3</sub> QDs with same or better size-dispersion (**Supplementary Fig. 19**). The latter include NCs capped with didodecyldimethylammonium bromide (DDAB) or OLAM/OA as used recently for NC superlattices<sup>9</sup>, as well as those capped with long-chain sulfobetaine zwitterionic ligands (3-(N,N-dimethyloctadecylammonio)propanesulfonate, ASC18) after size-selective precipitation<sup>47</sup>. Similarity of PL FWHM across these different shapes also evidences that the inhomogeneous broadening is not the cause for the "blurred" higher order absorption transitions in cuboidal QDs either. We thus turned to analyze the effect of the shape itself by computing a one-photon absorption cross-section (**Fig. 2c, 2d and Supplementary Fig. 20**). For this, the effective mass Approximation (EMA) was employed with the use of the energy-dependent effective mass to emulate the effect of full two-band coupling<sup>48</sup>. Beyond this, the electron-hole Coulomb interaction was included in a single-shot calculation (*i.e.* without self-consistency iteration, see details in **Supplementary note 2**). Compared to a perfect sphere, the cubic symmetry introduces perturbation that couples the spherical states of different angular momenta. This coupling leads to mixing between and splitting of the higher order absorption states, which results in the smoothing out of the absorption spectra, as observed experimentally. Furthermore, recent SAXS studies on cuboidal CsPbBr<sub>3</sub> NCs revealed up to 20% reduction in length along one of the cuboid edges (oblation), which further contributes to the splitting of higher order absorption states<sup>34,42</sup>. Particularly, going from the spherical shape to such an oblate cuboidal shape leads to the nearly complete flattening of the second and third absorption transitions.

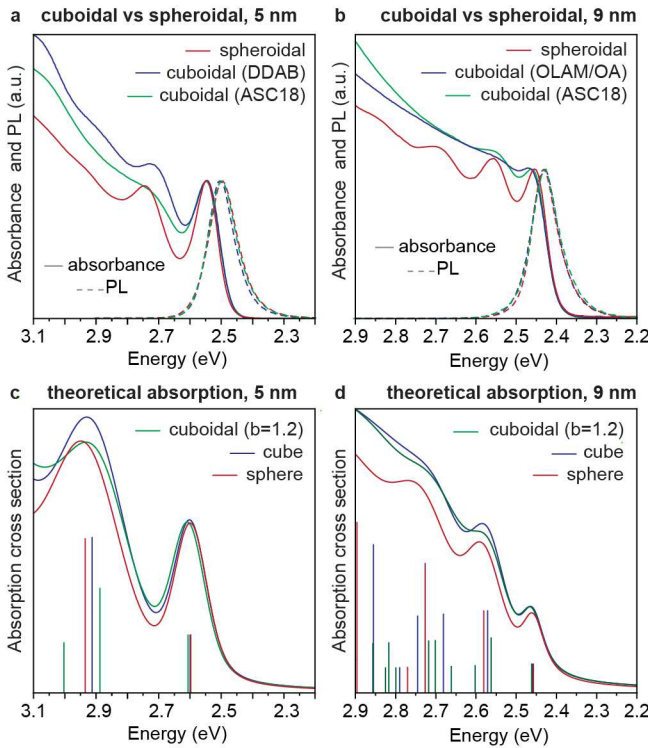


**Fig. 2 | The effect of QD shape on the absorption spectral features.** **a-b**, Experimental absorption and PL spectra of 5 nm and 9 nm cuboidal and spheroidal QDs. Monodisperse cuboidal QDs coated with DDAB<sup>9</sup>, OLAM/OA<sup>9</sup>, ACS18<sup>34</sup>. **c-d**, Calculated absorption spectra of both 5 and 9 nm QDs with different shapes using the effective mass approximation (EMA) with the inclusion of electron-hole Coulomb interaction in a single-shot calculation. For the cuboidal QD, an oblate shape was chosen with 20% shortening along one of the cube's edge (parameter  $b = 1.2$ ).

### Reaction mechanism.

We used *in-situ* optical absorption spectra to shed light onto the underlying chemical reactions and test reasoning on using solely neutral coordinating agent (TOPO) to prevent premature and uncontrolled conversion of  $\text{PbBr}_2$  into the  $\text{PbBr}_3^-$  solute.  $\text{PbBr}_2$  dissolves in TOPO forming a  $\text{PbBr}_2[\text{TOPO}]$  complex<sup>40</sup> that has a broad absorption peak around 4.4 eV (**Fig. 3a**), and its intensity change allows for monitoring the depletion of  $\text{PbBr}_2$  during the reaction. Only upon the injection of Cs-DOPA, does the  $\text{PbBr}_3^-$  appear on the course of 100 ms, evidenced as an additional peak emerging at lower energies (3.85 eV) (**Supplementary Fig. 21**), owing to the formation of a  $\text{PbBr}_3^-$  complex<sup>39,49</sup>. Once the accumulation of  $\text{PbBr}_3^-$  surpasses a nucleation threshold (supersaturation),  $\text{CsPbBr}_3$  QDs form (on the order of seconds, **Fig. 3b**). Whereas more conventional ligands for  $\text{CsPbBr}_3$  QDs, such as OA or OLAM, react with the  $\text{PbBr}_2[\text{TOPO}]$  complex<sup>40</sup>, free DOPA on its own does not (**Supplementary Fig. 22**). As the only counter-ion available to  $\text{PbBr}_3^-$  is

$\text{Cs}^+$ , we assume the formation of a  $\text{Cs}[\text{PbBr}_3]$  complex (tight ionic pair) as the concentration of  $\text{PbBr}_3^-$  species scales with Cs-DOPA concentration (**Supplementary Fig. 23a**). A  $\text{Cs}[\text{PbBr}_3]$  complex might be additionally coordinated by TOPO. Importantly, a higher TOPO concentration suppresses the formation of  $\text{Cs}[\text{PbBr}_3]$ , indicating that its formation is in equilibrium (**Supplementary Fig. 23b**) with more stable  $\text{PbBr}_2[\text{TOPO}]$  species. Particularly, an injection of additional TOPO after the initial Cs-DOPA injection decomposes  $\text{Cs}[\text{PbBr}_3]$  complex back into  $\text{PbBr}_2$  species (**Supplementary Fig. 24**).

An overall precursor-to-QDs path is depicted in **Fig. 3c**. We illustrate the effect of TOPO-driven  $\text{PbBr}_2:\text{Cs}[\text{PbBr}_3]$  equilibrium on the formation of  $\text{CsPbBr}_3$  QDs for a stoichiometric  $\text{PbBr}_2:\text{Cs-DOPA} = 3:2$  reaction by plotting *in-situ* monitored  $\text{PbBr}_2$ ,  $\text{Cs}[\text{PbBr}_3]$  and  $\text{CsPbBr}_3$  concentrations (**Fig. 3d**). An immediate decrease of  $\text{PbBr}_2$  concentration upon injection of Cs-DOPA is accompanied by the formation of  $\text{Cs}[\text{PbBr}_3]$ . As the reaction progresses,  $\text{Cs}[\text{PbBr}_3]$  complexes are converted into  $\text{CsPbBr}_3$  QDs nuclei, and both  $\text{PbBr}_2$  and  $\text{Cs}[\text{PbBr}_3]$  species are proportionally consumed, but remain present, in line with the  $\text{PbBr}_2:\text{Cs}[\text{PbBr}_3]$  equilibrium. The stoichiometric conversion  $3\text{PbBr}_2 \rightarrow 2\text{PbBr}_3^- + \text{Pb}^{2+}$  is confirmed by subtracting  $\text{Cs}[\text{PbBr}_3]$  and  $\text{CsPbBr}_3$  concentrations yielding the  $\text{PbDOPA}_2$  concentration. The reaction is eventually reaching a close to 100% yield (**Supplementary Fig. 25**). The rate-limiting step in this reaction is the conversion of the  $\text{Cs}[\text{PbBr}_3]$  intermediate into  $\text{CsPbBr}_3$ . A reaction with a four-fold excess of  $\text{PbBr}_2$  compared to Cs-DOPA (**Supplementary Fig. 26**) shows that the  $\text{Cs}[\text{PbBr}_3]$  complex solely acts as an intermediate for the  $\text{CsPbBr}_3$  QDs and is not stable on its own. The  $\text{PbBr}_2:\text{Cs}[\text{PbBr}_3]$  equilibrium self-limits the available amount  $\text{Cs}[\text{PbBr}_3]$  for both the nucleation, as well as the subsequent growth of  $\text{CsPbBr}_3$  QDs. The separation of nucleation and growth – a prerequisite for the narrow size dispersion - can be seen by comparing the QD concentration vs. the  $\text{CsPbBr}_3$  molar concentration evolution (**Fig. 3e and SI video 3**). The self-limiting equilibrium mechanism also explains the larger QD size and lower reaction speed with increasing TOPO concentration. The equilibrium shifts towards  $\text{PbBr}_2$ , reducing the available quantity of  $\text{Cs}[\text{PbBr}_3]$  for the nucleation and hence decreasing the number of nuclei (and the final QD concentration, **Fig. 3f**), whilst the overall yield remains relatively unchanged (**Supplementary Fig. 27**). For instance, a four-fold increase in TOPO concentration translates into the size increase from 3.5 to 8.7 nm, corresponding to a 14-fold increase in QD volume. The QD concentration correspondingly drops 15 times. Additional experiments confirming the self-limiting equilibrium mechanism are described in **Supplementary note 3**.

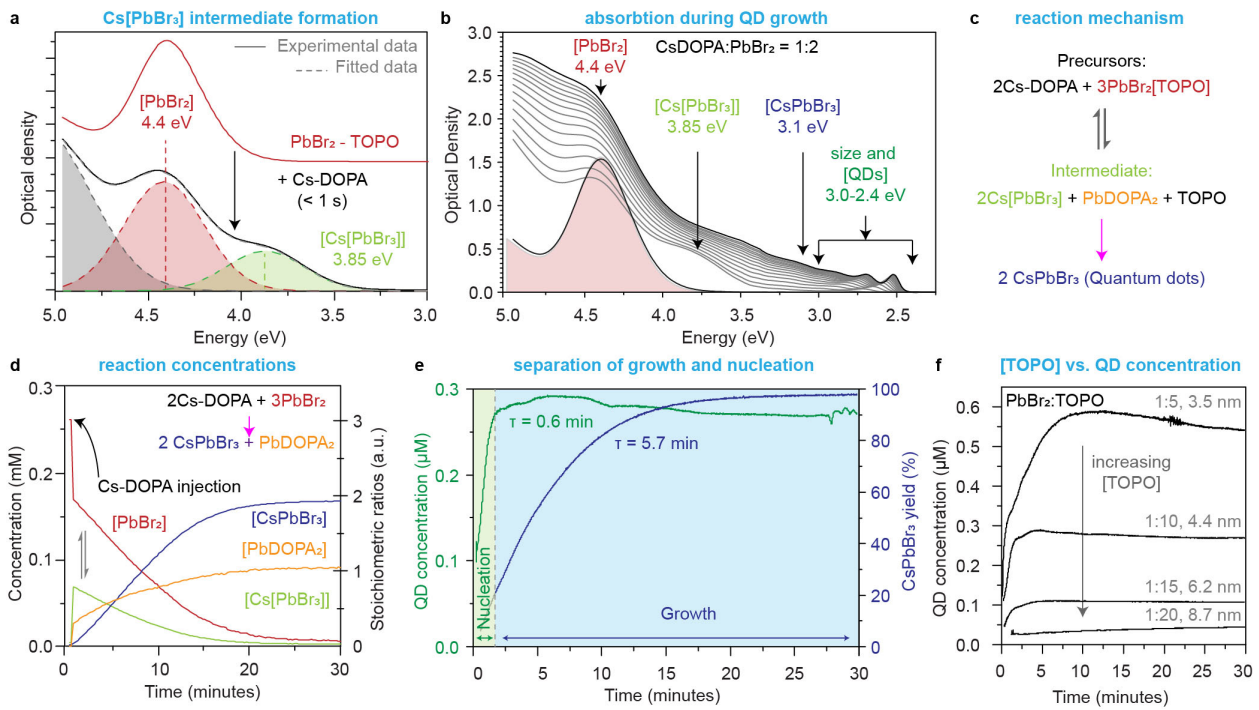


**Fig. 3 | In-situ observation of the precursors-to-CsPbBr<sub>3</sub> QDs conversion.** **a**, PbBr<sub>2</sub>-TOPO solution before and within 5 seconds after the injection of Cs-DOPA. **b,c**, Typical evolution of the absorption spectra from PbBr<sub>2</sub> through Cs[PbBr<sub>3</sub>] monomer and CsPbBr<sub>3</sub> QDs and the corresponding reaction path. **d**, Temporal evolution of precursors' and reaction products' concentrations for a stoichiometric reaction (2:3 Cs-DOPA:PbBr<sub>2</sub>), wherein both the PbBr<sub>2</sub> precursor and the Cs[PbBr<sub>3</sub>] intermediate are consumed upon the formation of CsPbBr<sub>3</sub> QDs. PbBr<sub>2</sub> and Cs[PbBr<sub>3</sub>] exist in equilibrium, as both are present until PbBr<sub>2</sub> is consumed. **e**, Effective separation of nucleation and growth, as well as absence of QD coalescence or Ostwald ripening is apparent from the QD concentration evolution and the respective reaction yield. **f**, QD concentration vs. time dependence at different TOPO concentrations. Higher TOPO quantities suppress the available Cs[PbBr<sub>3</sub>] monomer and hence the number of nuclei.

### Optical properties of CsPbBr<sub>3</sub> QDs.

Contrasting the many investigations of higher-order excitonic transitions and their size- and shape-dependencies in CdSe and PbS QDs<sup>50,51</sup>, the assignment of corresponding datasets for CsPbBr<sub>3</sub> QDs remains very limited as, typically, only the lowest two transitions (1s-1s and 1p-1p) are reported<sup>34,52</sup>. In the present study, the first four excitonic transitions are readily resolved both *in-situ* (see **Fig. 4a** and **Supplementary Video 4** as well as **Extended Data Fig. 5** for various final QD sizes) and *ex-situ* linear absorption spectra (**Fig. 4b**). Size dependencies captured by 25'000 *in-situ* experimental spectra recorded for 2.5-11 nm QDs (**Fig. 4c** exemplifies) are retained also in the purified QDs (**Fig. 4d**). To assign the absorption features, the specific excitonic transitions were calculated using a two-band *k.p* model<sup>34,52</sup>. The

Coulomb interaction was included under the self-consistent Hartree-Fock approximation. More details on the theoretical formalism are discussed in the **Supplementary Note 2**. For the 1s-1s, 1p-1p, 1d-1d and 1f-1f transitions, we find a good agreement of the theoretical and experimental transition energies, plotted relative to the first excited state (1s-1s) as a function of their first excited state energies (**Fig. 4f**)<sup>50</sup>. The spheroidal CsPbBr<sub>3</sub> QDs optically behave as confined model systems with symmetrical electron and hole manifolds, owing to their approximately equal effective masses. The theoretical absorption spectrum is then obtained from calculations of the oscillator strength for all allowed transitions using second-order many-body perturbation theory, which allows partial incorporation of correlation effects in the electron-photon interaction<sup>48,53</sup>. Each transition was broadened with a normalized Voigt line-shape and the results for all transitions were added to obtain the final absorption spectra shown, for instance, for 7.0 nm (**Fig. 4g and Extended Data Fig. 5**). This model was further extended for a broad range of temperatures between 14 K and 300 K, as shown in **Extended Data Fig. 6**. More discussion on the broadening mechanisms is found in **Supplementary Note 4** and **Supplementary Fig. 28**. The calculated low-temperature absorption spectrum was compared to the PL excitation (PLE) spectrum at 14 K (**Fig. 4h**). Whereas only one 1p-1p state transition is expected and observed at room-temperature, the narrowing of the absorption features upon cooling to 14 K reveals two 1p-1p contributions, separated by ca. 70 meV. This splitting is observed in temperature-dependent absorption spectra for various QD sizes (**Extended Data Fig. 7b and 7c**) and was previously ascribed to the shape-asymmetry in cuboidal QDs (oblation in one direction)<sup>34,52</sup>. A likewise observation in isotropic spheroidal QDs calls for other considerations such as anisotropies of the effective mass of electrons or holes, stemming from the orthorhombic crystal structure of the CsPbBr<sub>3</sub><sup>54,55</sup>. Such anisotropic effects were already inferred from electrical characteristics<sup>56</sup>. Inclusion of 10-15% of anisotropy in the electron hole mass gives rise to the experimentally found splitting of the 1p-1p transition of the magnitude found experimentally (**Extended Data Fig. 8 and Supplementary Fig. 29 and 30**). The splitting of the 1p states potentially experiences a fairly complex dependence on the QD size and temperature; see further discussion in **Supplementary Note 5**.

Simultaneous *in-situ* acquisition of both absorption and PL spectra allowed us to study the inherent size-dependent Stokes shift (**Extended Data Fig. 1 and Supporting Videos 1 and 5**) with excellent energy accuracy (standard deviation of only about 2% in the range of 4-10 nm, **Extended Data Fig. 9**,

**Supplementary Fig. 31).** The measured Stokes shift agrees with recent calculations that assume an intrinsic confined hole state with size-dependent alignment above the valence band maximum<sup>57</sup>.

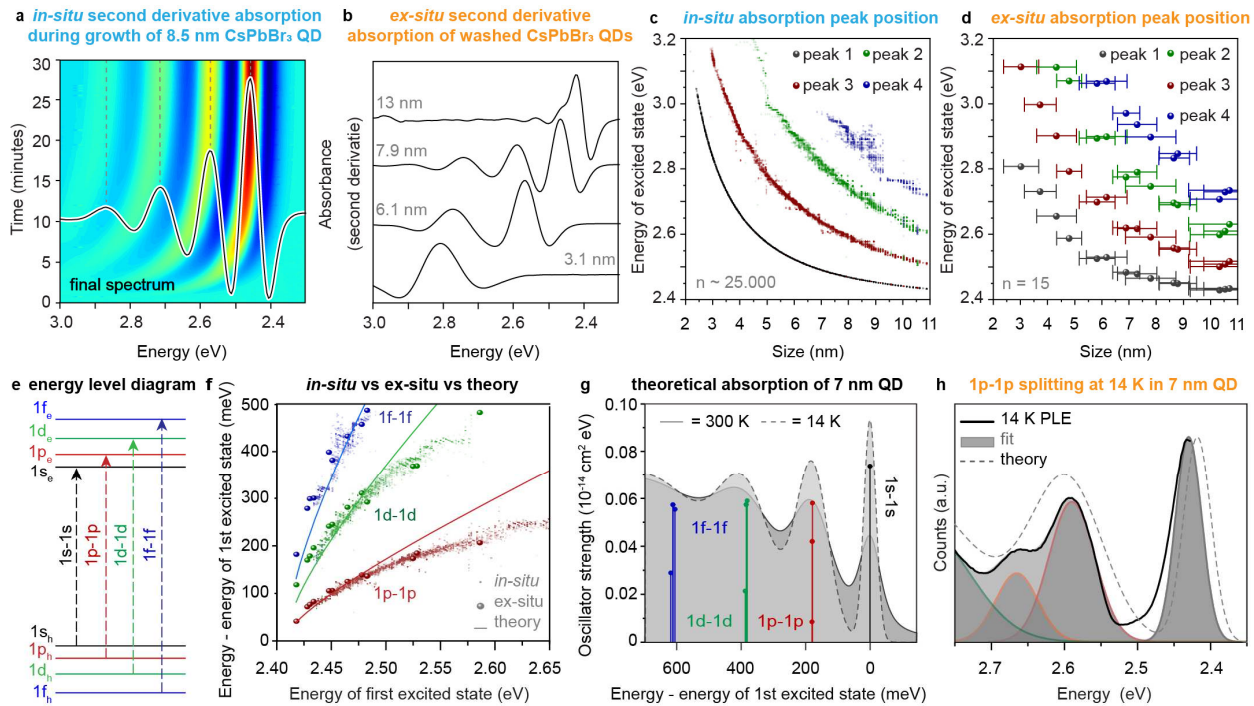


**Fig. 4 | Excitonic transitions in CsPbBr<sub>3</sub> QDs seen with *in-* and *ex-situ* spectroscopy corroborated with theoretical calculations.** **a**, Typical second derivative of the absorption during the growth of CsPbBr<sub>3</sub> QDs, featuring up to four transitions that can be extracted using a peak finding algorithm. **b**, Second derivative absorption spectra for purified QDs. **c**, A compilation of the extracted *in-situ* transition energy values across several syntheses ( $n \sim 25000$  individual absorption spectra). **d**, Similar data set obtained *ex-situ* from 15 different QD sizes. **e**, Energy level diagram used for the two-band  $k.p$  theory with Hartree-Fock level description of the Coulomb interaction<sup>48,53</sup>. **f**, Comparison of experimental relative absorption transitions and theoretical calculated states. **g**, Theoretical absorption spectrum in which the electron-photon interaction is considered within the framework of second-order many-body perturbation theory with the corresponding peak assignment. **h**, 14 K PLE spectra revealing splitting of the 1p-1p transition due to slight anisotropy in effective masses.

#### Extension to FAPbBr<sub>3</sub> and MAPbBr<sub>3</sub> QDs.

We then sought to extend the synthesis methodology to hybrid small organic-inorganic LHP QDs (**Fig. 5**). FAPbBr<sub>3</sub> QDs were synthesized by replacing Cs<sub>2</sub>CO<sub>3</sub> with FA-acetate and DOPA with a mixture of DOPA and OA. FAPbBr<sub>3</sub> QDs were observed to form an order of magnitude faster compared to CsPbBr<sub>3</sub> QDs (minute-scale, see **Fig. 5a** for *in-situ* absorption in the synthesis of 7 nm FAPbBr<sub>3</sub> QDs). Analogous experiments with MA-acetate gave rise to a size-series of monodisperse MAPbBr<sub>3</sub> NCs, albeit with further

reduction of the synthesis time to *ca.* 10 s (**Fig. 5e**). Such a pronounced effect of the A-site cation on the reaction rate agrees with the proposed reaction mechanism (**Fig. 3c**), wherein coordination of A-cation to

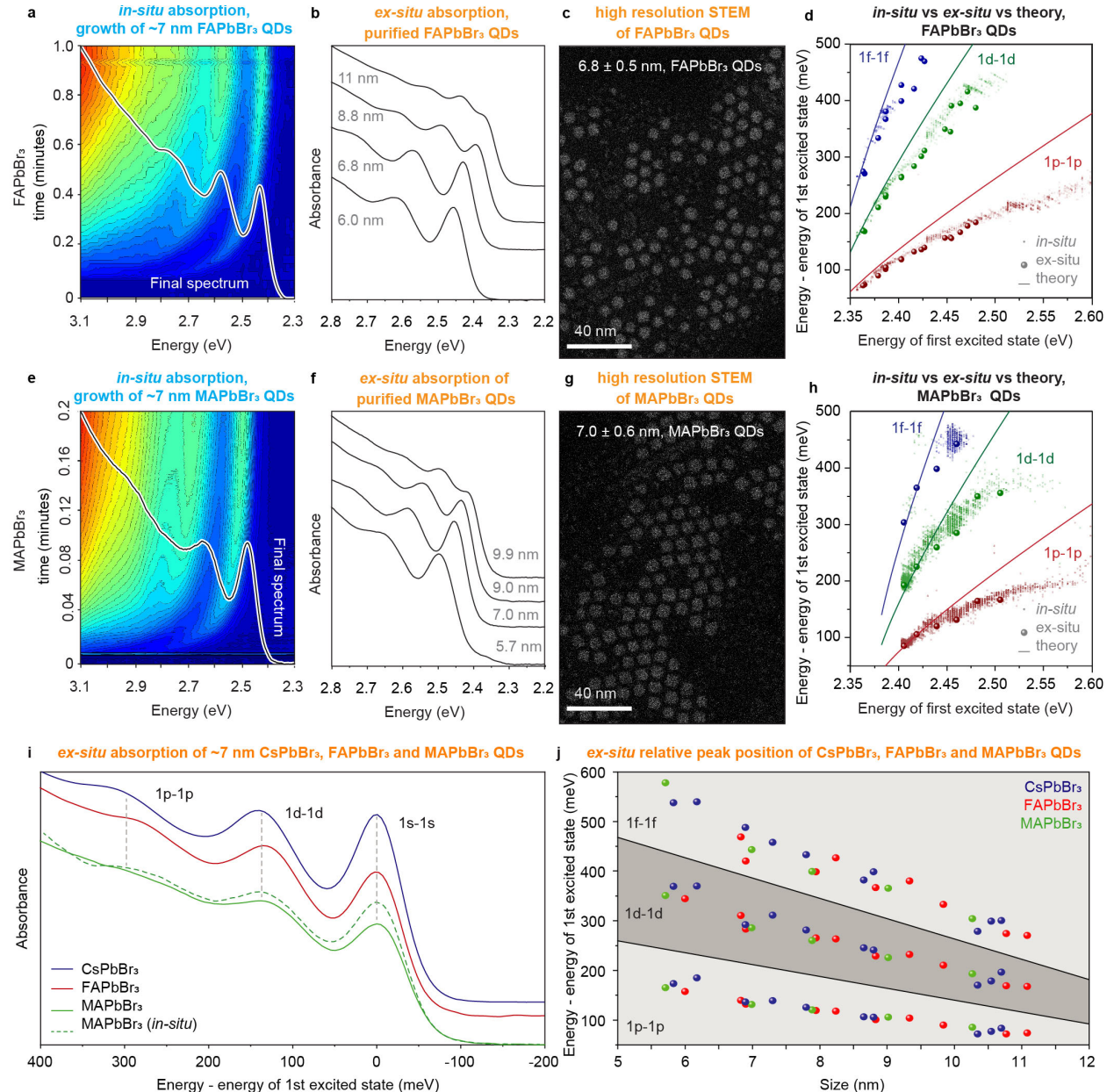


**Fig. 5 | Monodisperse FAPbBr<sub>3</sub> and MAPbBr<sub>3</sub> QDs and comparison with CsPbBr<sub>3</sub> QDs.** **a,e** *In-situ* spectra during the formation of 7-nm QDs. **b,f** Absorption spectra of isolated series. **c,g** STEM images of *ca.* 7 nm QDs. **d,h** *In-situ*, *ex-situ* and calculated excitonic transition energies plotted with respect to their first excitonic transition energy.. **i**, Absorption spectra of *ca.* 7-nm CsPbBr<sub>3</sub>, FAPbBr<sub>3</sub> and MAPbBr<sub>3</sub> QDs with matched at the 1s-1s transition energy. **j**, Experimental size-dependent relative peak position of CsPbBr<sub>3</sub>, FAPbBr<sub>3</sub> and MAPbBr<sub>3</sub> QDs.

$\text{PbBr}_3^-$  was hypothesized to govern the stability and hence reactivity of these transient species. Size series of 6-11 nm lecithin-capped  $\text{FAPbBr}_3$  and  $\text{MAPbBr}_3$  QDs (**Fig. 5b and 5f**), which are found to be quasi-spherical in shape (**Fig. 5c and 5g**), are analogous to  $\text{CsPbBr}_3$  QDs. These hybrid LHP NCs feature narrow size dispersion of under 10% and well-resolved, machine-readable excitonic peaks in both *in-situ* and *ex-situ* measurements (see **Fig 5d and 5h**). See further examples in **Extended Data Fig. 10a and b** and additional TEM images in **in Supplementary Fig. 32**. Notably, the faster formation kinetics does not jeopardize the utility of the synthesis, as the QD size control is accomplished at a full reaction yield by adjusting the concentrations, not growth time.

We then sought to compare all three LHP homologues as they feature an analogous Pb-halide octahedral framework. As illustrated in **Fig. 5i**, the 7-nm  $\text{CsPbBr}_3$ ,  $\text{FAPbBr}_3$  and  $\text{MAPbBr}_3$  QDs exhibit nearly identical absorption spectra, when matching the positions of their first excitonic transition. Moreover, across the experimental and theoretical size-series, all three materials exhibit the same effect of quantum-confinement on higher-order excitonic transitions (**Fig. 5j and Supplementary Fig. 33**).

In sum, we have introduced a synthesis methodology that (i) can conveniently handle the precursor-monomer equilibrium and hence the formation kinetics of small LHP QDs at room temperature, inherently separating the nucleation and growth, and (ii) yields scalable quantities of such QDs at full reaction yield. The slower overall reaction rate allows for convenient *in-situ* optical parametric screening and, in future, also structural characterization. This work provides avenues for studying strongly quantum confined LHP QDs with inherently conspicuous excitonic features.

## References

1. Protesescu, L. *et al.* Nanocrystals of Cesium Lead Halide Perovskites ( $\text{CsPbX}_3$ , X = Cl, Br, and I): Novel Optoelectronic Materials Showing Bright Emission with Wide Color Gamut. *Nano Lett.* **15**, 3692-3696 (2015).
2. Zhang, F. *et al.* Brightly Luminescent and Color-Tunable Colloidal  $\text{CH}_3\text{NH}_3\text{PbX}_3$  (X = Br, I, Cl) Quantum Dots: Potential Alternatives for Display Technology. *ACS Nano* **9**, 4533-4542 (2015).
3. Protesescu, L. *et al.* Monodisperse Formamidinium Lead Bromide Nanocrystals with Bright and Stable Green Photoluminescence. *J. Am. Chem. Soc.* **138**, 14202-14205 (2016).
4. Kovalenko, M. V., Protesescu, L. & Bodnarchuk, M. I. Properties and Potential Optoelectronic Applications of Lead Halide Perovskite Nanocrystals. *Science* **358**, 745-750 (2017).
5. Akkerman, Q. A., Rainò, G., Kovalenko, M. V. & Manna, L. Genesis, Challenges and Opportunities for Colloidal Lead Halide Perovskite Nanocrystals. *Nat. Mater.* **17**, 394-405 (2018).
6. Dey, A. *et al.* State of the Art and Prospects for Halide Perovskite Nanocrystals. *ACS Nano* **15**, 10775-10981 (2021).

7. Tamarat, P. *et al.* The Ground Exciton State of Formamidinium Lead Bromide Perovskite Nanocrystals Is a Singlet Dark State. *Nat. Mater.* **18**, 717-724 (2019).
8. Park, Y.-S., Guo, S., Makarov, N. S. & Klimov, V. I. Room Temperature Single-Photon Emission from Individual Perovskite Quantum Dots. *ACS Nano* **9**, 10386-10393 (2015).
9. Cherniukh, I. *et al.* Perovskite-Type Superlattices from Lead Halide Perovskite Nanocubes. *Nature* **593**, 535-542 (2021).
10. Dong, Y. *et al.* Bipolar-Shell Resurfacing for Blue LEDs Based on Strongly Confined Perovskite Quantum Dots. *Nat. Nanotechnol.* **15**, 668-674 (2020).
11. Kim, Y.-H. *et al.* Comprehensive Defect Suppression in Perovskite Nanocrystals for High-Efficiency Light-Emitting Diodes. *Nat. Photonics* **15**, 148-155 (2021).
12. Hassan, Y. *et al.* Ligand-Engineered Bandgap Stability in Mixed-Halide Perovskite LEDs. *Nature* **591**, 72-77 (2021).
13. Wang, Y.-K. *et al.* All-Inorganic Quantum-Dot LEDs Based on a Phase-Stabilized  $\alpha$ -CsPbI<sub>3</sub> Perovskite. *Angew. Chem. Int.* **60**, 16164-16170 (2021).
14. Yoon, H. C. *et al.* Highly Efficient Wide-Color-Gamut QD-Emissive LCDs Using Red and Green Perovskite Core/Shell QDs. *J. Mater. Chem. C* **6**, 13023-13033 (2018).
15. Ko, Y.-H., Jalalah, M., Lee, S.-J. & Park, J.-G. Super Ultra-High Resolution Liquid-Crystal-Display Using Perovskite Quantum-Dot Functional Color-Filters. *Sci. Rep.* **8**, 12881 (2018).
16. He, Z., Zhang, C., Dong, Y. & Wu, S.-T. Emerging Perovskite Nanocrystals-Enhanced Solid-State Lighting and Liquid-Crystal Displays. *Cryst.* **9**, 59 (2019).
17. Su, R. *et al.* Room-Temperature Polariton Lasing in All-Inorganic Perovskite Nanoplatelets. *Nano Lett.* **17**, 3982-3988 (2017).
18. Schlaus, A. P. *et al.* How Lasing Happens in CsPbBr<sub>3</sub> Perovskite Nanowires. *Nat. Commun.* **10**, 265 (2019).
19. Li, S. *et al.* Water-Resistant Perovskite Nanodots Enable Robust Two-Photon Lasing in Aqueous Environment. *Nat. Commun.* **11**, 1192 (2020).
20. Zhang, Q. *et al.* Halide Perovskite Semiconductor Lasers: Materials, Cavity Design, and Low Threshold. *Nano Lett.* **21**, 1903-1914 (2021).
21. Chen, Q. *et al.* All-Inorganic Perovskite Nanocrystal Scintillators. *Nature* **561**, 88-93 (2018).
22. Gandini, M. *et al.* Efficient, Fast and Reabsorption-Free Perovskite Nanocrystal-Based Sensitized Plastic Scintillators. *Nat. Nanotechnol.* **15**, 462-468 (2020).
23. Meinardi, F. *et al.* Doped Halide Perovskite Nanocrystals for Reabsorption-Free Luminescent Solar Concentrators. *ACS Energy Lett.* **2**, 2368-2377 (2017).
24. Wei, M. *et al.* Ultrafast Narrowband Exciton Routing within Layered Perovskite Nanoplatelets Enables Low-Loss Luminescent Solar Concentrators. *Nat. Energy* **4**, 197-205 (2019).
25. Wu, J. *et al.* Efficient and Stable Thin-Film Luminescent Solar Concentrators Enabled by near-Infrared Emission Perovskite Nanocrystals. *Angew. Chem. Int.* **59**, 7738-7742 (2020).
26. Chen, W. *et al.* Giant Five-Photon Absorption from Multidimensional Core-Shell Halide Perovskite Colloidal Nanocrystals. *Nat. Commun.* **8**, 15198 (2017).
27. Becker, M. A. *et al.* Long Exciton Dephasing Time and Coherent Phonon Coupling in CsPbBr<sub>2</sub>Cl Perovskite Nanocrystals. *Nano Lett.* **18**, 7546-7551 (2018).
28. Rainò, G. *et al.* Single Cesium Lead Halide Perovskite Nanocrystals at Low Temperature: Fast Single-Photon Emission, Reduced Blinking, and Exciton Fine Structure. *ACS Nano* **10**, 2485-2490 (2016).
29. Utzat, H. *et al.* Coherent Single-Photon Emission from Colloidal Lead Halide Perovskite Quantum Dots. *Science* **363**, eaau7392 (2019).
30. Yin, C. *et al.* Bright-Exciton Fine-Structure Splittings in Single Perovskite Nanocrystals. *Phys. Rev. Lett.* **119**, 026401 (2017).
31. Cho, K. *et al.* Luminescence Fine Structures in Single Lead Halide Perovskite Nanocrystals: Size Dependence of the Exciton–Phonon Coupling. *Nano Lett.* **21**, 7206-7212 (2021).
32. Rainò, G. *et al.* Superfluorescence from Lead Halide Perovskite Quantum Dot Superlattices. *Nature* **563**, 671-675 (2018).
33. Mattiotti, F. *et al.* Thermal Decoherence of Superradiance in Lead Halide Perovskite Nanocrystal Superlattices. *Nano Lett.* **20**, 7382-7388 (2020).
34. Krieg, F. *et al.* Monodisperse Long-Chain Sulfobetaine-Capped CsPbBr<sub>3</sub> Nanocrystals and Their Superfluorescent Assemblies. *ACS Cent. Sci.* **7**, 135-144 (2021).

35. De Roo, J. *et al.* Highly Dynamic Ligand Binding and Light Absorption Coefficient of Cesium Lead Bromide Perovskite Nanocrystals. *ACS Nano* **10**, 2071-2081 (2016).
36. Dong, Y. *et al.* Precise Control of Quantum Confinement in Cesium Lead Halide Perovskite Quantum Dots Via Thermodynamic Equilibrium. *Nano Lett.* **18**, 3716-3722 (2018).
37. Imran, M. *et al.* Shape-Pure, Nearly Monodispersed  $\text{CsPbBr}_3$  Nanocubes Prepared Using Secondary Aliphatic Amines. *Nano Lett.* **18**, 7822-7831 (2018).
38. Almeida, G. *et al.* Role of Acid–Base Equilibria in the Size, Shape, and Phase Control of Cesium Lead Bromide Nanocrystals. *ACS Nano* **12**, 1704-1711 (2018).
39. Hui, J. *et al.* Unveiling the Two-Step Formation Pathway of  $\text{Cs}_4\text{PbBr}_6$  Nanocrystals. *Chem. Mater.* **32**, 4574-4583 (2020).
40. Almeida, G. *et al.* The Phosphine Oxide Route toward Lead Halide Perovskite Nanocrystals. *J. Am. Chem. Soc.* **140**, 14878-14886 (2018).
41. Shynkarenko, Y. *et al.* Direct Synthesis of Quaternary Alkylammonium-Capped Perovskite Nanocrystals for Efficient Blue and Green Light-Emitting Diodes. *ACS Energy Lett.* **4**, 2703-2711 (2019).
42. Krieg, F. *et al.* Stable Ultraconcentrated and Ultradilute Colloids of  $\text{CsPbX}_3$  ( $X = \text{Cl}, \text{Br}$ ) Nanocrystals Using Natural Lecithin as a Capping Ligand. *J. Am. Chem. Soc.* **141**, 19839-19849 (2019).
43. Akkerman, Q. A. *et al.* Tuning the Optical Properties of Cesium Lead Halide Perovskite Nanocrystals by Anion Exchange Reactions. *J. Am. Chem. Soc.* **137**, 10276-10281 (2015).
44. Nedelcu, G. *et al.* Fast Anion-Exchange in Highly Luminescent Nanocrystals of Cesium Lead Halide Perovskites ( $\text{CsPbX}_{3\text{ls}}$ ,  $X = \text{Cl}, \text{Br}, \text{I}$ ). *Nano Lett.* **15**, 5635-5640 (2015).
45. Imran, M. *et al.* Benzoyl Halides as Alternative Precursors for the Colloidal Synthesis of Lead-Based Halide Perovskite Nanocrystals. *J. Am. Chem. Soc.* **140**, 2656-2664 (2018).
46. Zhang, B. *et al.* Stable and Size Tunable  $\text{CsPbBr}_3$  Nanocrystals Synthesized with Oleylphosphonic Acid. *Nano Lett.* **20**, 8847-8853 (2020).
47. Krieg, F. *et al.* Colloidal  $\text{CsPbX}_3$  ( $X = \text{Cl}, \text{Br}, \text{I}$ ) Nanocrystals 2.0: Zwitterionic Capping Ligands for Improved Durability and Stability. *ACS Energy Lett.* **3**, 641-646 (2018).
48. Sercel, P. C., Lyons, J. L., Bernstein, N. & Efros, A. L. Quasicubic Model for Metal Halide Perovskite Nanocrystals. *J. Chem. Phys.* **151**, 234106 (2019).
49. Yoon, S. J., Stamplecoskie, K. G. & Kamat, P. V. How Lead Halide Complex Chemistry Dictates the Composition of Mixed Halide Perovskites. *J. Phys. Chem. Lett.* **7**, 1368-1373 (2016).
50. Norris, D. J. & Bawendi, M. G. Measurement and Assignment of the Size-Dependent Optical Spectrum in CdSe Quantum Dots. *Phys. Rev. B* **53**, 16338-16346 (1996).
51. Andreev, A. D. & Lipovskii, A. A. Anisotropy-Induced Optical Transitions in PbSe and PbS Spherical Quantum Dots. *Phys. Rev. B* **59**, 15402-15404 (1999).
52. Shcherbakov-Wu, W. *et al.* Temperature-Independent Dielectric Constant in  $\text{CsPbBr}_3$  Nanocrystals Revealed by Linear Absorption Spectroscopy. *J. Phys. Chem. Lett.* **12**, 8088-8095 (2021).
53. Nguyen, T. P. T., Blundell, S. A. & Guet, C. One-Photon Absorption by Inorganic Perovskite Nanocrystals: A Theoretical Study. *Phys. Rev. B* **101**, 195414 (2020).
54. Sakuma, T. *et al.* Low-Energy Excitation in  $\text{CsPbX}_3$  ( $X=\text{Cl}, \text{Br}$ ). *Solid State Ion.* **154-155**, 237-242 (2002).
55. Traoré, B. *et al.* Efficient and Accurate Calculation of Band Gaps of Halide Perovskites with the Tran-Blaha Modified Becke-Johnson Potential. *Phys. Rev. B* **99**, 035139 (2019).
56. Zhang, P. *et al.* Anisotropic Optoelectronic Properties of Melt-Grown Bulk  $\text{CsPbBr}_3$  Single Crystal. *J. Phys. Chem. Lett.* **9**, 5040-5046 (2018).
57. Brennan, M. C. *et al.* Origin of the Size-Dependent Stokes Shift in  $\text{CsPbBr}_3$  Perovskite Nanocrystals. *J. Am. Chem. Soc.* **139**, 12201-12208 (2017).
58. Chao, L. *et al.* Room-Temperature Molten Salt for Facile Fabrication of Efficient and Stable Perovskite Solar Cells in Ambient Air. *Chem* **5**, 995-1006 (2019).
59. Maes, J. *et al.* Light Absorption Coefficient of  $\text{CsPbBr}_3$  Perovskite Nanocrystals. *J. Phys. Chem. Lett.* **9**, 3093-3097 (2018).
60. Jones, L. *et al.* Smart Align—a New Tool for Robust Non-Rigid Registration of Scanning Microscope Data. *Adv. Struct. Chem. Imaging.* **1**, 8 (2015).

61. Shibata, K. *et al.* Exciton Localization and Enhancement of the Exciton–LO Phonon Interaction in a CsPbBr<sub>3</sub> Single Crystal. *J. Phys. Chem. C* **124**, 18257–18263 (2020).
62. Ramade, J. *et al.* Exciton-Phonon Coupling in a CsPbBr<sub>3</sub> Single Nanocrystal. *Appl. Phys. Lett.* **112**, 072104 (2018).
63. Yang, Z. *et al.* Impact of the Halide Cage on the Electronic Properties of Fully Inorganic Cesium Lead Halide Perovskites. *ACS Energy Lett.* **2**, 1621–1627 (2017).
64. Wang, X., Wang, Q., Chai, Z. & Wu, W. The Thermal Stability of FAPbBr<sub>3</sub> Nanocrystals from Temperature-Dependent Photoluminescence and First-Principles Calculations. *RSC Adv.* **10**, 44373–44381 (2020).

## Methods

**Chemicals.** Lead(II) bromide (PbBr<sub>2</sub>, 99.999%), zinc chloride (ZnCl<sub>2</sub>, 98%), cesium carbonate (Cs<sub>2</sub>CO<sub>3</sub>, 99.9%), formamidinium acetate (99%), methylamine (33 wt% in ethanol), acetic acid (99.5%), hexane (≥99%), diisooctylphosphinic acid (DOPA, 90%), oleic acid (OA, 90%) and acetone (ACE, ≥99.5%) were purchased from Sigma Aldrich. n-Octane (min. 99%) and lecithin (>97% from soy) were purchased from Carl Roth. Trioctylphosphine oxide (TOPO, min. 90%) was purchased from Strem Chemicals. All chemicals were used as received. Methyl ammonium acetate was synthesized by reacting methylamine with acetic acid as described in Ref<sup>58</sup>.

**Stock solutions.** PbBr<sub>2</sub> stock solution (0.04 M), as well as ZnCl<sub>2</sub> solution used for anion exchange, was prepared by dissolving PbBr<sub>2</sub> or ZnCl<sub>2</sub> (1 mmol) and TOPO (5 mmol) in octane (5 mL) at 120 °C, followed by dilution with hexane (20 mL). The Cs-DOPA solution (0.02 M) was prepared by mixing Cs<sub>2</sub>CO<sub>3</sub> (100 mg) with DOPA (1 mL) and octane (2 mL) at 120 °C, followed by dilution with hexane (27 mL). The FA-DOPA stock solution (0.02 M) was prepared by loading formamidinium acetate (64 mg), DOPA (3 mL), OA (3 mL) and octane (5 mL) at 120 °C, followed by dilution with hexane (20 mL). This solution was diluted further five times prior to the synthesis. The MA-DOPA stock solutions was prepared analogously to FA-DOPA solution using methylammonium acetate. The lecithin stock solution (~0.13 M) was prepared by dissolving 0.5 gram of lecithin in hexane (10 mL). This solution was diluted 10 times in the case of FAPbBr<sub>3</sub> and MAPbBr<sub>3</sub> QDs. The TOPO stock solution (0.2 M) was prepared by dissolving TOPO (4 mmol) in hexane (20 mL). The DOPA stock solution was prepared by diluting DOPA 40 times in hexane. The ZnCl<sub>2</sub> solutions used for anion solution was prepared in the same way as the PbBr<sub>2</sub> solutions, with the replaced of PbBr<sub>2</sub> with ZnCl<sub>2</sub>. All stock solutions were filtered through 0.2 µL PTFE filter prior to use.

**Synthesis of CsPbBr<sub>3</sub>, FAPbBr<sub>3</sub> and MAPbBr<sub>3</sub> QDs.** In an 8 ml vial, PbBr<sub>2</sub> and TOPO stock solutions were combined along with additional hexane. Under vigorous stirring, a desired volume of Cs/MA/FA-DOPA stock solution was injected. Specific volumes of solutions are tabulated in Supplementary Tables 1 and 2 for all reactions presented in this work.

**Ligand exchange and QD purification.** Once the spectral evolution is plateaued at a final bandgap value, a stock solution of lecithin is added (the volume being equivalent to the A-cation stock solution used in the respective QD synthesis). After half a minute, a ca. 3-fold excess of an antisolvent (acetone for CsPbBr<sub>3</sub>; ethyl acetate:acetonitrile 2:1 for FAPbBr<sub>3</sub>, and MAPbBr<sub>3</sub>) was added and the QDs were isolated by centrifuging at 19970 g for 2 minutes and redispersed in hexane.

**In-situ absorption and photoluminescence (PL) setup.** The reactions were carried out in a modified Thorlabs CVH100 cuvette holder. The absorption spectra were recorded with an Ocean Optics deuterium-tungsten light source (DH-2000-BAL-TTL-24V) and a Thorlabs CCS200/M spectrometer. For collecting PL spectra, a bifurcated optical fiber was used in a front-face configuration, minimizing the PL reabsorption. PL was excited with a Convoy 53 UV flashlight and recorded with a Thorlabs CCS200/M spectrometer. The time resolution in these measurements was set to 50 µs.

**In-situ absorption in the UV range.** For the higher-energy absorption studies (precursor formation and higher-order absorption transitions), covering both the UV range down to 200 nm, the reaction was carried out in a Jasco V670 spectrometer using a 2MAG cuvetteMIXdrive 1 cuvette stirring plate equipped with a cuvette magnetic stirrer. This allowed for a time resolution of about 20 seconds per spectrum.

**Ex-situ absorption and photoluminescence (PL) spectroscopy.** Room-temperature PL spectra of purified QDs were recorded with a Fluorolog iHR 320 Horiba Jobin Yvon with an excitation at 350 nm. Absorption spectra were recorded on a Jasco V670 spectrometer.

**Low-temperature PLE and absorption setup.** PLE spectra were acquired with a Picoquant FluoTime300 fluorescence spectrometer equipped with a Xe lamp for excitation and a photomultiplier tube for detection. Monochromators, in both the excitation and detection path, serve to select and scan the excitation and emission wavelength. An ARS closed-cycle He cryostat in combination with a Lakeshore temperature controller were employed to control the sample temperature. The QD samples were spin-coated as thin films on Si/SiO<sub>2</sub> substrates and measured in vacuum. PLE spectra were recorded for an emission

wavelength set to 35 meV with respect to the PL peak; qualitatively similar spectra were observed also when the emission wavelength was set to the PL peak. The low-temperature absorption was recorded in the same cryostat system, but with an Ocean Optics deuterium-tungsten lamp (DH-2000-BAL-TTL-24V) as white light source and a Thorlabs CCS200/M spectrometer as detector.

**Data analysis and fitting.** Custom-developed batch analysis scripts (written in Python) were employed. Here, the low-energy portion of both the absorption and PL spectra were fitted with a partial Gaussian to extract the first absorption and PL peak positions. The first absorption peak position was used to calculate the size<sup>34</sup>. The molar concentration of CsPbBr<sub>3</sub> was calculated from the absorbance at 3.1 eV<sup>59</sup>. The precursor concentrations were calculated by fitting the absorption data with Gaussians at 4.4 eV (PbBr<sub>2</sub>) and 3.85 eV (PbBr<sub>3</sub><sup>-</sup>) after a CsPbBr<sub>3</sub> background subtraction. The concentration of Pb(DOPA)<sub>2</sub> was determined by subtracting the PbBr<sub>2</sub>, PbBr<sub>3</sub><sup>-</sup> and CsPbBr<sub>3</sub> concentration from the starting PbBr<sub>2</sub> concentration. The higher-order absorption transitions were determined via a peak finding function on the negative second derivative of the absorption spectra. Further details are given in the Supplementary note 1.2.

**Small and wide-angle X-ray scattering (SAXS/WAXS) measurements.** The SAXS/WAXS experiment was performed at beamline P21.2 at Petra III (DESY) synchrotron in Hamburg. X-ray photon energies of 37.5 keV (0.0331 nm) with VAREX XRD4343CT detector and a sample-to-detector distance of 1.5 m (for WAXS) and 15 m (SAXS) were employed. These distances allowed us to probe a q-range between 16 nm<sup>-1</sup> and 58 nm<sup>-1</sup> for the WAXS and between 0.15 nm<sup>-1</sup> and 2.2 nm<sup>-1</sup> for the SAXS. The q-range and the scattering intensity were calibrated with LaF<sub>6</sub>, while absolute intensities were obtained by calibrating with glassy carbon.

**Transmission electron microscopy measurements (TEM).** TEM images were obtained using a JEOL JEM-1400 Plus microscope operating at 120 kV. Bright-field and dark-field scanning TEM (STEM) imaging was performed on a JEOL JEM2200FS microscope equipped with a Schottky field emission electron gun. High-angle annular dark-field scanning TEM (HAADF-STEM) images were collected at cryo-conditions (holder cooled with liquid nitrogen) on an aberration-corrected HD2700CS (Hitachi) operated at 200 kV with a point resolution of ca. 1 Å. HR ADF-STEM was carried out using a probe-aberration-corrected FEI Titan Themis operated at 300 kV employing a beam semi-convergence angle of 18 mrad and a beam current of

1 pA. Under the high-resolution acquisition conditions used, the dose per frame was about 50 electrons/ $\text{\AA}^2$ . Series of images of each particle were recorded and 8-10 frames were averaged for noise-reduction, warranting that the nanoparticles remained unchanged in the averaged frames. The frames were aligned using the non-rigid algorithm as implemented in SmartAlign<sup>60</sup>.

**Empirical modelling.** For the comparison between a sphere and a cube, EMA was employed together with a single-shot computation of Coulomb interaction. The correspondence  $L = \sqrt{3} R$  was made where  $L$  and  $R$  are the cube edge length and sphere radius, respectively. For the peak assignment and the absorption cross-section, assuming spherical symmetry, the two-band  $k.p$  model was used and the Coulomb interaction was treated using the Hartree-Fock approximation. Electron-photon interaction was computed within second-order many-body perturbation theory. The QD size is taken to be  $\sqrt{3} R_{eff}$  where  $R_{eff}$  is the effective sphere radius. More details can be found in **Supplementary Notes 2 and 4**.

## Acknowledgements

This work was financially supported by the European Union's through Horizon 2020 Research and innovation Programme through European Research Commission (ERC-CoG, agreement number 819740, project SCALE-HALO) and FET Open research and innovation action (grant agreement no. 899141, project PoLLOC) and US Air Force Office of Scientific Research (award number FA8655-21-1-7013). SAXS and WAXS measurements were carried out at beamline P21.2 at PETRA III at DESY, a member of the Helmholtz Association (HGF); we thank M. Blankenburg and U. Lienert for assistance during the measurements. The research leading to this result has been supported by the project CALIPSOplus under the Grant Agreement 730872 from the EU Framework Programme for Research and Innovation HORIZON 2020. We thank F. Krumeich and I. Cherniukh for HAADF-STEM measurements and F. Krieg and I. Cherniukh for providing reference cuboidal CsPbBr<sub>3</sub> NCs.

## Author contributions

Q.A.A. performed the synthesis and optical characterization, with the contributions from P.W., F.B and D.N.D. T.P.T.N, C.K. and J.E. carried out theoretical calculations. S.C.B performed the low-temperature PLE measurements. F.M. carried out the WAXS and SAXS experiments. R.E. conducted electron

microscopy. Q.A.A and M.V.K. wrote the manuscript, with input from all authors. M.V.K, C.K. and J.E. supervised the project.

**Competing financial interests:** The authors declare no competing financial interest.

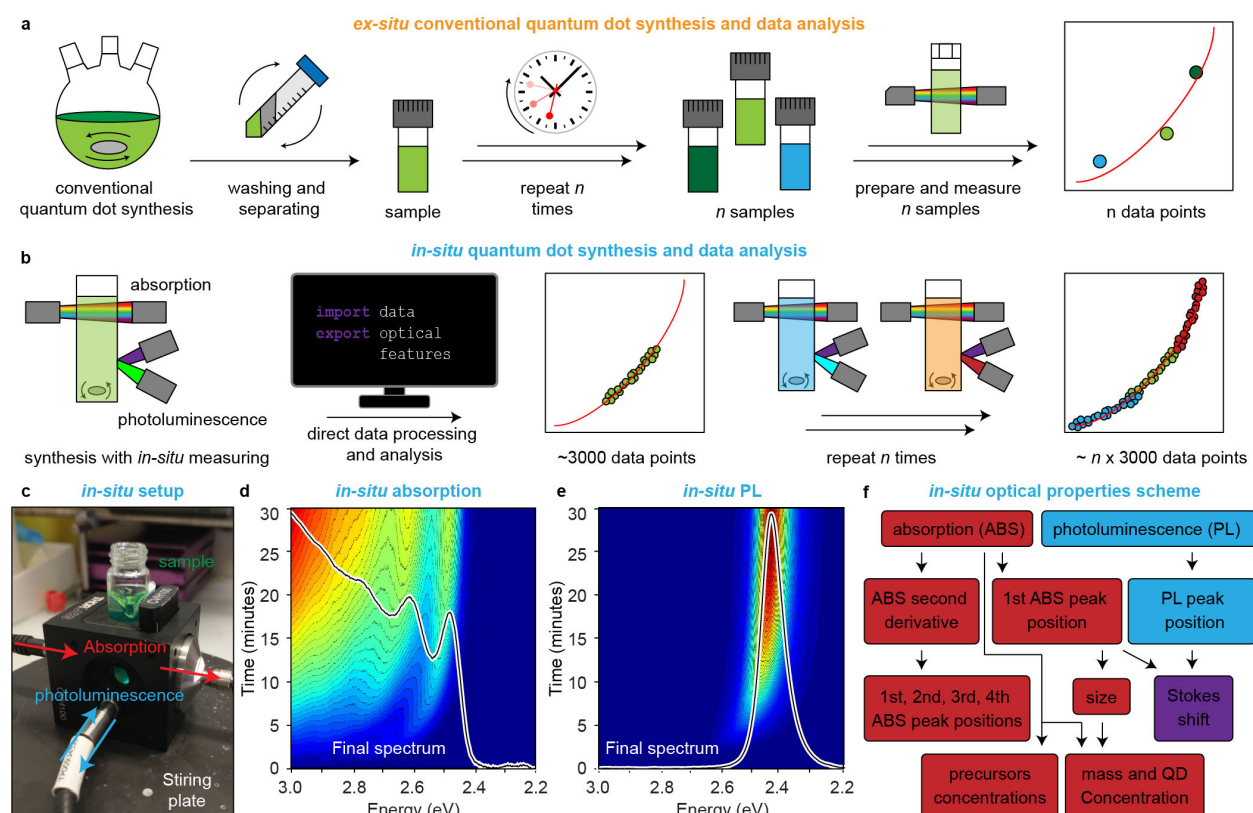
## Additional Information

**Supplementary Information** is available for this paper.

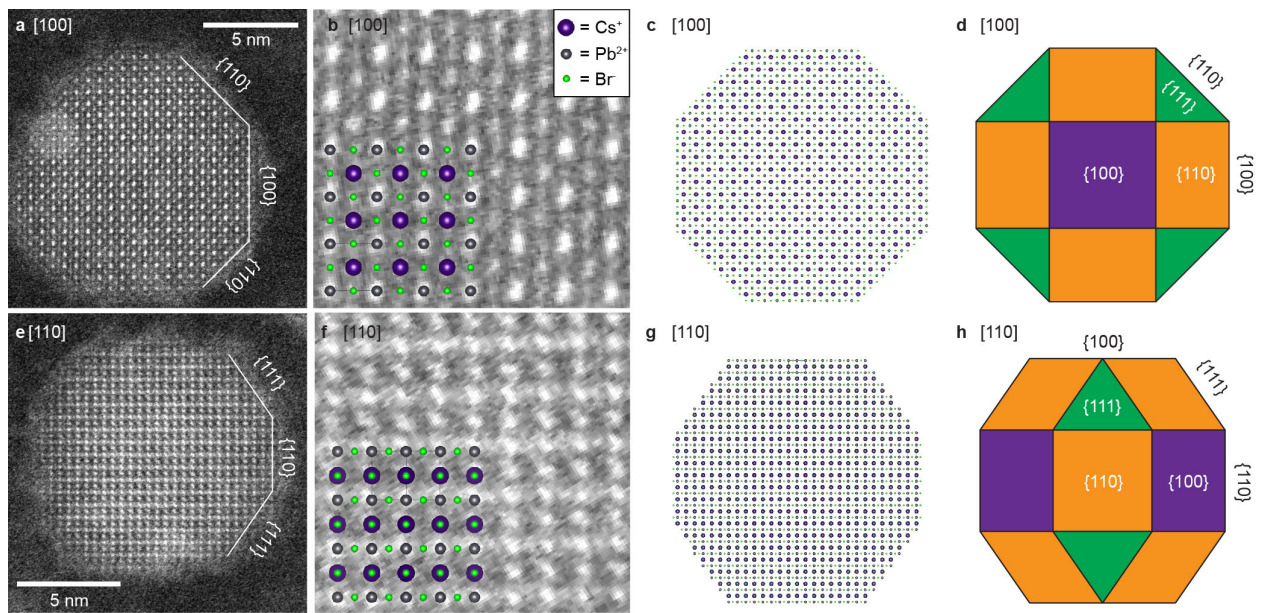
**Materials & Correspondence** Maksym V. Kovalenko ([mvkovalenko@ethz.ch](mailto:mvkovalenko@ethz.ch))

**Correspondence and requests for materials** should be addressed to M.V.K.

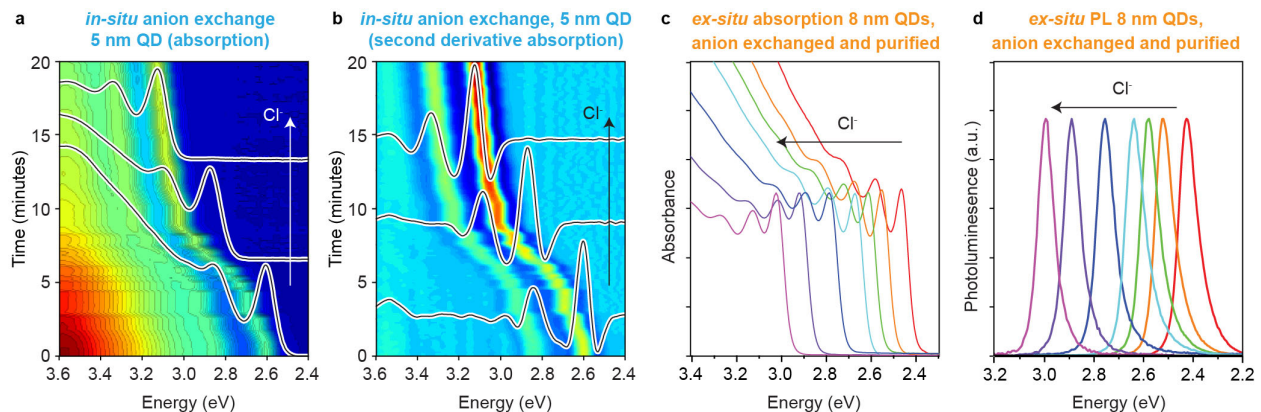
## Extended Data Figures



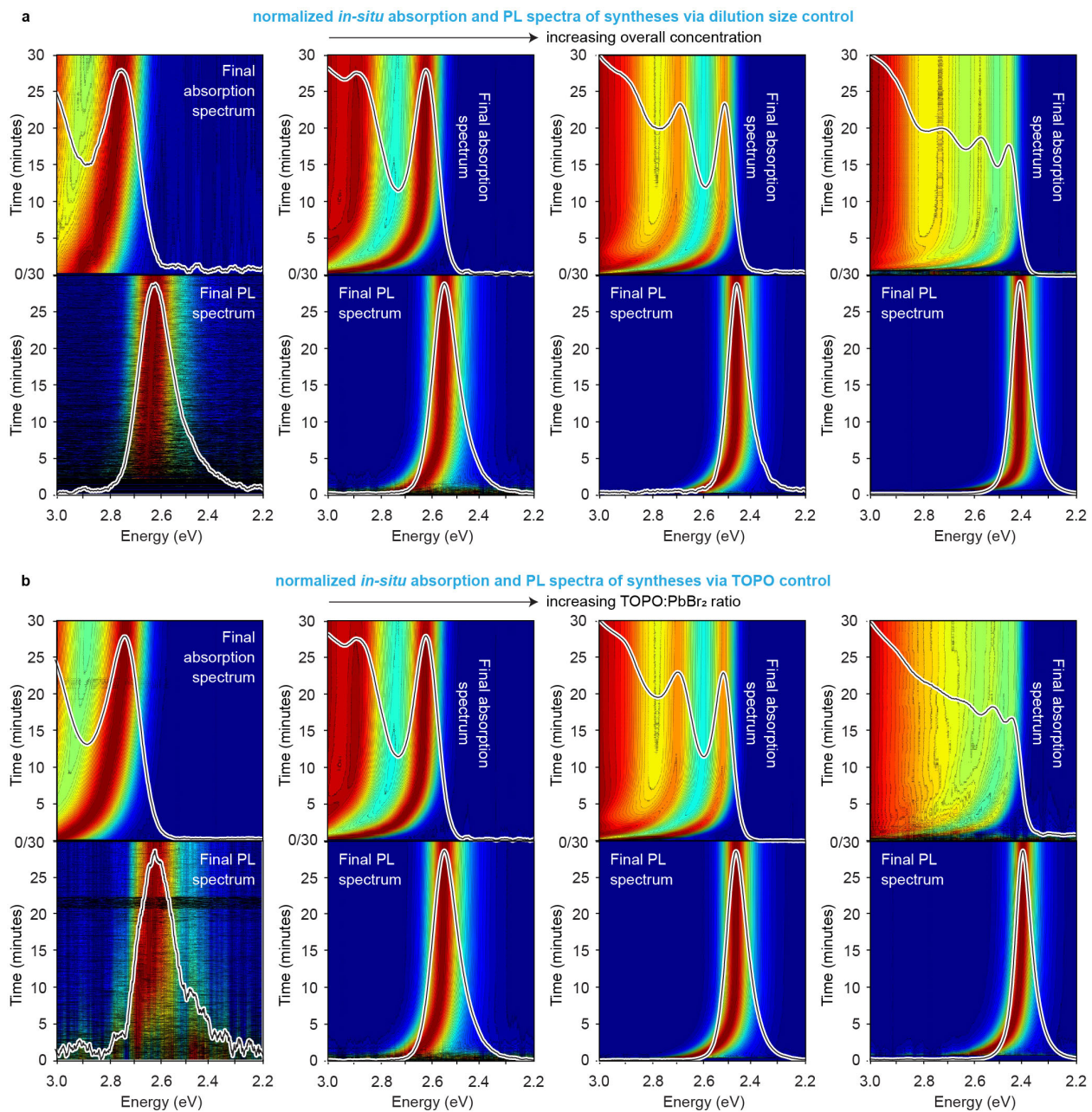
**Extended Data Fig. 1 | Comparison between *in-situ* and *ex-situ* data analysis and overview of *in-situ* measurements.** **a**, Schematic showing conventional *ex-situ* data acquisition and analysis. **b**, Schematic of *in-situ* acquisition and *in-situ* analysis. **c**, Setup for *in-situ* absorption and PL measurements. **d**, Example of *in-situ* absorption measurement with simultaneous **e**, *in-situ* PL measurement. **f**, Schematic overview of data analysis of *in-situ* absorption and PL data.



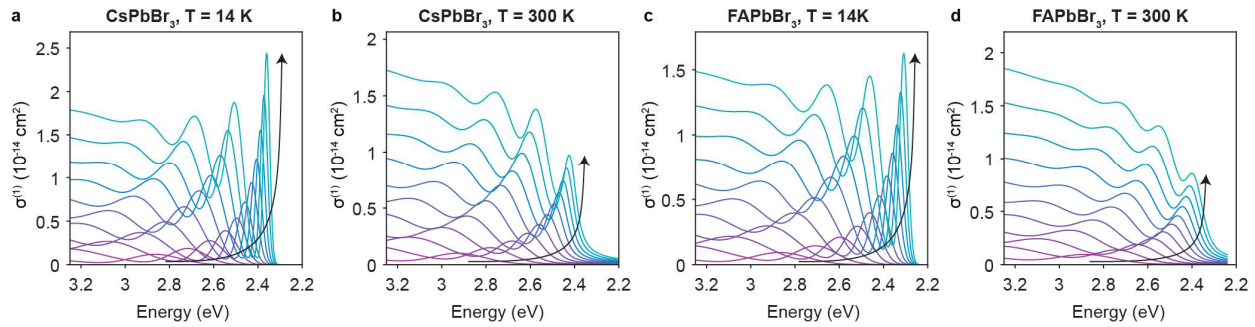
**Extended Data Fig. 2 | HR-STEM analysis of 12 nm  $\text{CsPbBr}_3$  QDs and their rhombicuboctahedral shape.** **a**, HR-STEM image of a single 12 nm QD in [100] orientation, showing truncation along {110} facets. **b**, Overlap of HR-STEM image and crystal lattice of  $\text{CsPbBr}_3$  along [100] axis. **c**, Graphic representation of 20x20x20 unit cell QD truncated along {110} and {111} facets shown along [100] axis. **d**, Simple graphical representation of rhombicuboctahedron shown along [100] axis. **e**, Single QD in [110] orientation, showing truncation along {111} facets. **f**, Overlap of HR-STEM image and crystal lattice of  $\text{CsPbBr}_3$  along [100] axis. **g**, graphic representation of 20x20x20 unit cell QD truncated along {110} and {111} facets shown along [110] axis. **h**, Graphical representation of rhombicuboctahedron shown along [110] axis.



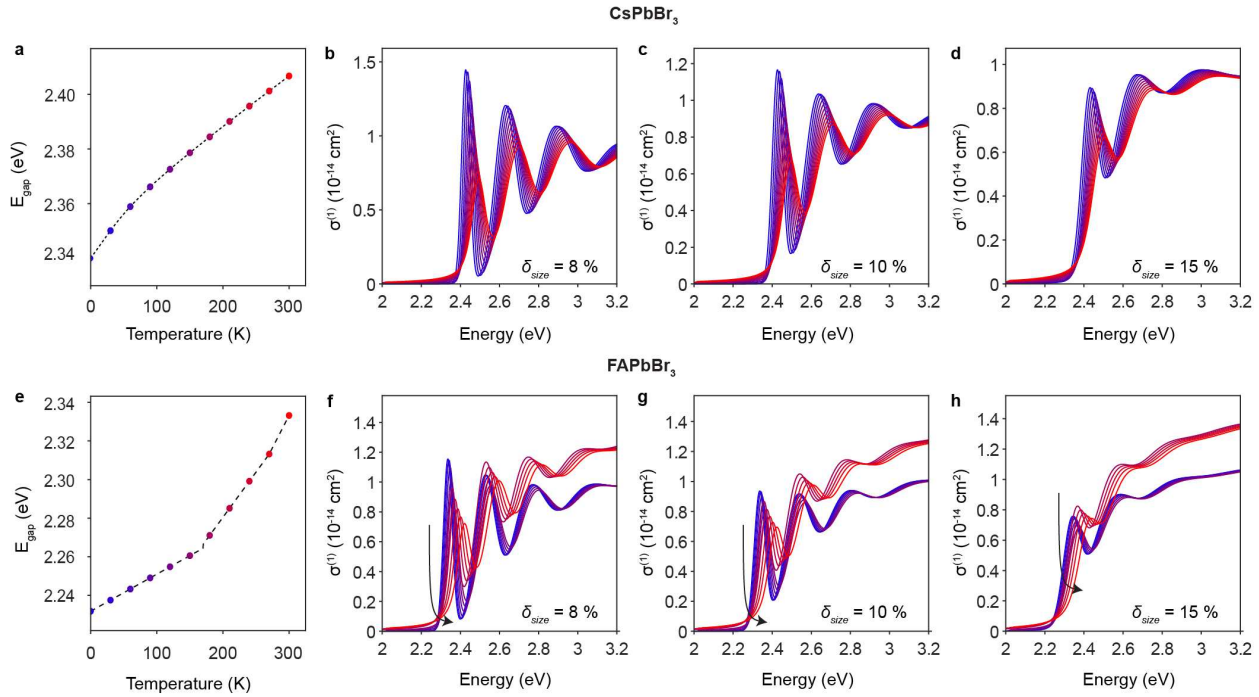
**Extended Data Fig. 3 | CsPbBr<sub>3</sub> to CsPbCl<sub>3</sub> QDs by anion-exchange.** **a**, *In-situ* recorded absorption spectra of 5 nm CsPbBr<sub>3</sub> QDs undergoing controlled Cl<sup>-</sup> anion exchange via dropwise addition of Cl<sup>-</sup> precursor, with respective second derivative shown in **b**. **c**, Absorption spectra of a series of purified 8 nm CsPb(Br:Cl)<sub>3</sub> QDs with well-resolved higher-order absorption peaks, which remain preserved after the anion-exchange reaction and purification. **d**, Respective PL spectra of QD sample shown in panel c.



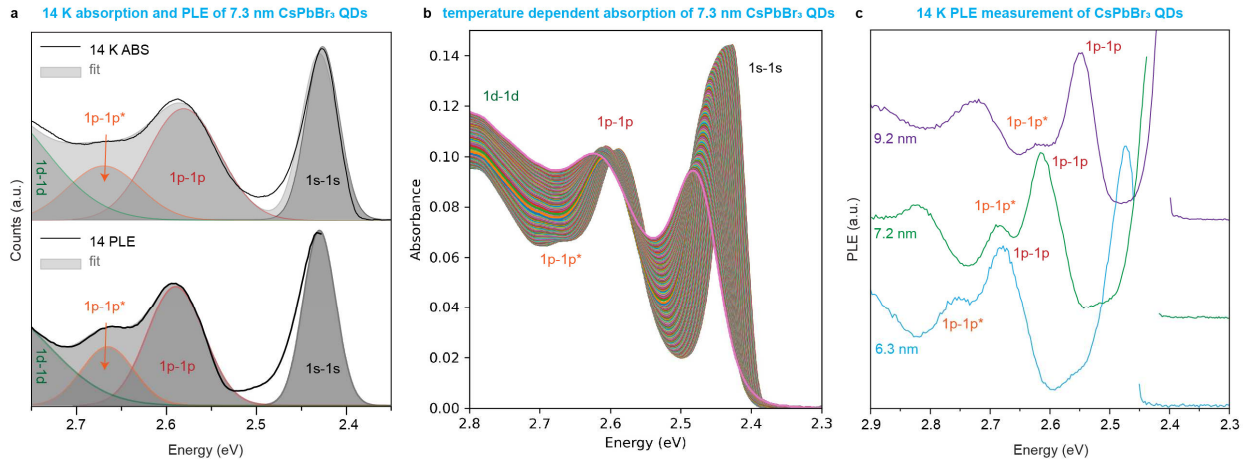
**Extended Data Fig. 4 | *In-situ* measurements of CsPbBr<sub>3</sub> QDs synthesized under different growth conditions.** **a**, CsPbBr<sub>3</sub> QD size-control by adjusting the overall concentrations. **b**, Size-tuning of CsPbBr<sub>3</sub> QDs by increasing the TOPO:PbBr<sub>2</sub> ratio. All absorption spectra are normalized at 3 eV for better visual guide of the spectral evolution.



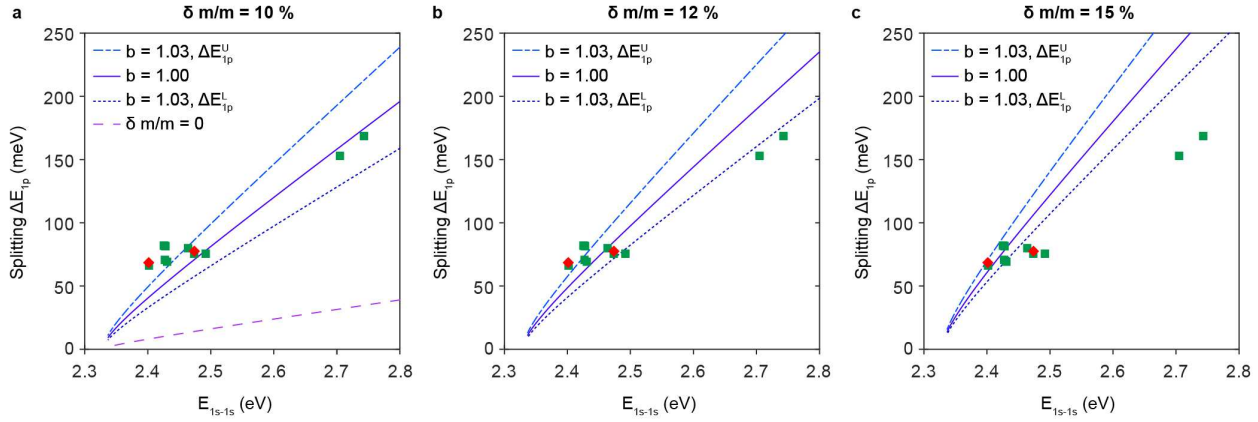
**Extended Data Fig. 5 | Theoretical one-photon absorption cross-section  $\sigma^{(1)}$  ( $10^{-14}$  cm $^2$ ) versus energy (eV) for different sizes using spherical k.p model.** The direction of increasing size, where  $L = 3.0 - 8.0$  nm with size step equal to 0.5 nm, is indicated by a black arrow. **a** and **b**, CsPbBr<sub>3</sub>; **c** and **d**, FAPbBr<sub>3</sub>. The absorption spectra were calculated at 14 K (panels **a** and **c**) and at 300 K (panels **b** and **d**). The broadening parameters used for CsPbBr<sub>3</sub> and FAPbBr<sub>3</sub> QDs are discussed in **Supplementary Note 4**.



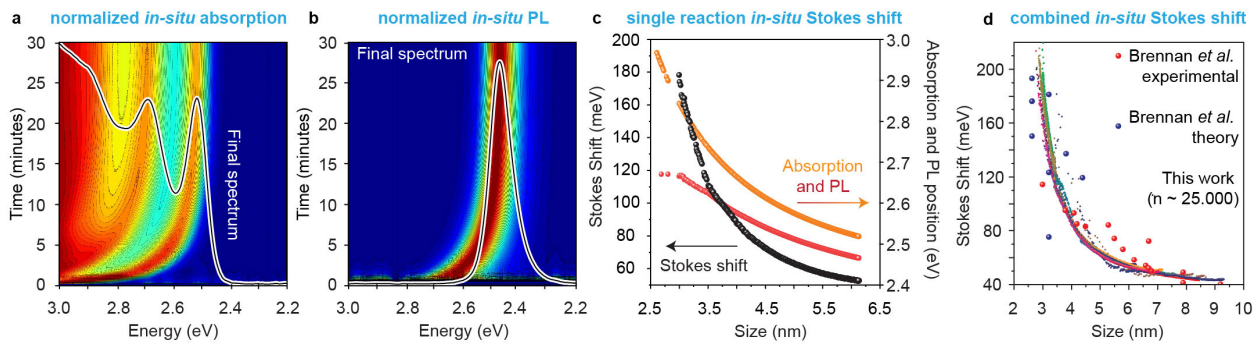
**Extended Data Fig. 6 | Temperature dependence of one-photon absorption cross-section spectrum  $\sigma^{(1)}$  ( $10^{-14}$  cm $^2$ ) versus energy (eV) in spherical k.p model.** **a-d**, CsPbBr<sub>3</sub>; **e-h**, FAPbBr<sub>3</sub>. QD size is  $L = 7.0$  nm for both cations. The arrows denote direction of increasing temperature. Each calculated spectrum corresponds to the temperature represented by each dot on the leftmost panels. The size dispersion  $\delta_{size}$  is 8%, 10% and 15% from left to right (panels **b** to **d** for CsPbBr<sub>3</sub>, panels **f** to **h** for FAPbBr<sub>3</sub>). For CsPbBr<sub>3</sub>, the temperature-dependent electronic band gap is modelled as in Ref <sup>61</sup>. Using  $A_{linear} = 0.339$  meV/K,<sup>61</sup> and  $E_{LO} = 16$  meV,<sup>62</sup> the choice of  $A_{LO} = 30$  meV correctly reproduces the absorption band gap of CsPbBr<sub>3</sub> as measured by Yang *et al*<sup>63</sup>. The change of  $E_{gap}$  of FAPbBr<sub>3</sub> versus temperature was fitted using linear function for the data from Wang *et al*<sup>64</sup>. The modelling of line shape can be found in **Supplementary Note 4**.



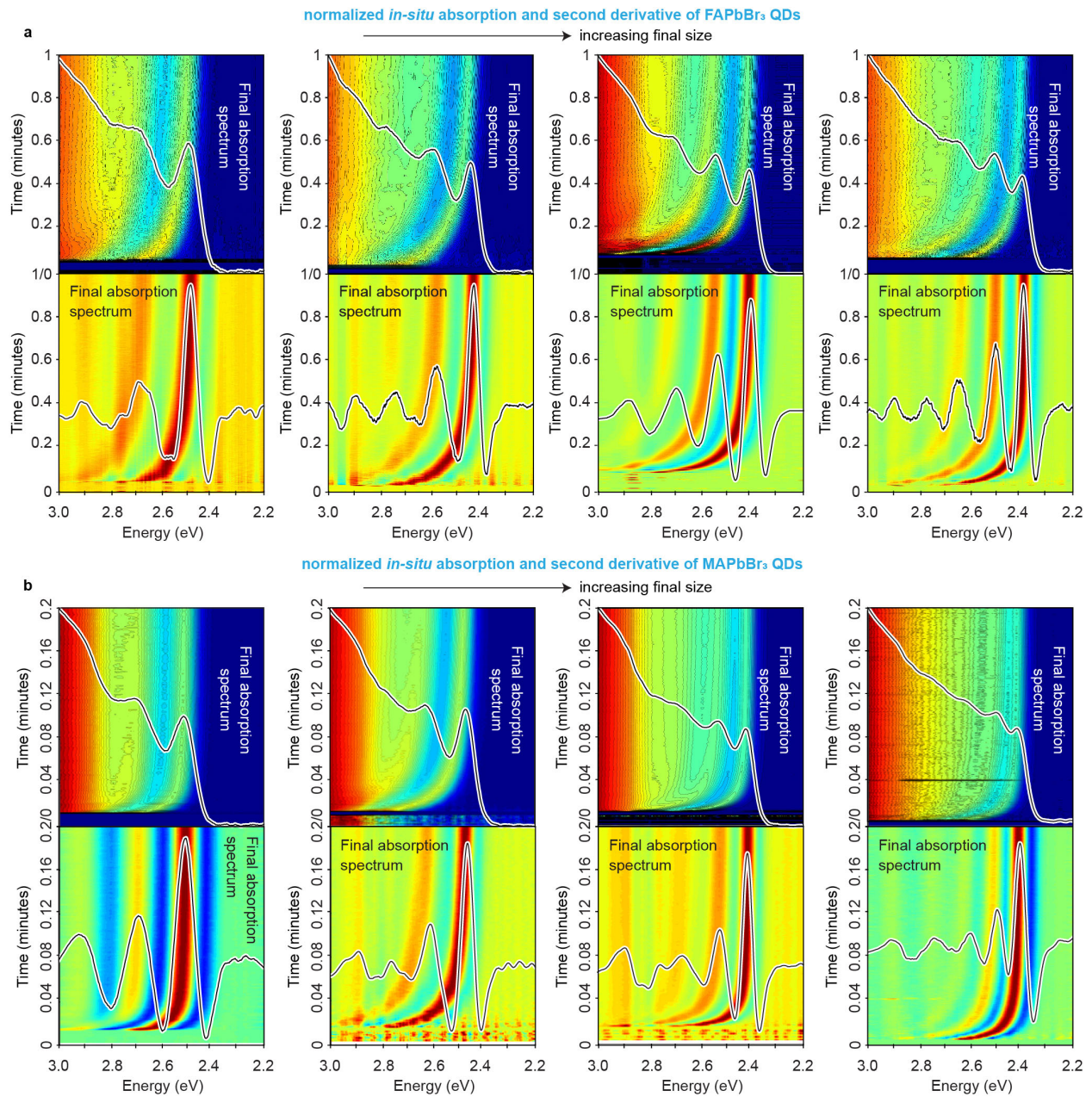
**Extended Data Fig. 7 | Additional low-temperature absorption and PLE data.** **a**, 14 K absorption and PLE spectra with their respective multigaussian fit, demonstrating splitting of 1p-1p states. The higher-energy 1p-1p has been marked with\*. **b**, Temperature-dependent absorption spectra of 7.3 nm  $\text{CsPbBr}_3$  QD from room temperature to 14 K, showing the appearance of the second high-energy p-p peak around 2.65–2.70 eV. **b**, 14 K PLE measurements of  $\text{CsPbBr}_3$  QDs in the range of 6–9 nm, all showing a second 1p-1p transition.



**Extended Data Fig. 8| Energy splitting  $\Delta E_{1p}$  (meV) between the 1p-1p transitions versus the first absorption peak  $E_{1s-1s}$  (eV).** Experimental data points were extracted using second derivative (green square) or multi-Gaussian fit (red diamond) from the low-temperature absorption spectra. The theoretical lines in panels a to c were done using the dimensionless mass variation  $\delta m/m = 10\%$ ,  $12\%$  and  $15\%$ , respectively. Aspect ratio  $b = 1.03$ .  $\Delta E_{1p}^U$  (light blue, dash dotted line): upper bound;  $\Delta E_{1p}^{\delta m/m}$  (solid blue): without shape anisotropy, i.e.  $b = 1.00$ ;  $\Delta E_{1p}^L$  (dark blue, dotted line): lower bound. For panel a,  $\Delta E_{1p}^b$  (purple dash line) was computed without mass anisotropy, i.e.  $\delta m/m = 0$ ,  $b = 1.03$ , to demonstrate the effect of only shape anisotropy.



**Extended Data Fig. 9 | Overview of *in-situ* Stokes shift measurements.** **a**, Normalized absorption spectra of 6.2 nm CsPbBr<sub>3</sub> QD and **b**, corresponding PL spectra. Here, the spectra are normalized at 3 eV to better demonstrate the growth. **c**, *In-situ* absorption and PL peak positions and the respective calculated Stokes shift as a function of size during the measurement shown in **a-b**. **d**, Size-dependent Stokes shift study of over 25.000 different spectra from 12 different reactions, compared to Brennan *et al*<sup>57</sup>.



**Extended Data Fig. 10 | *In-situ* absorption measurements of FAPbBr<sub>3</sub> and MAPbBr<sub>3</sub> QDs for different final sizes.** The synthesis conditions are found in **Supplementary Tables 1 and 2**. **a**, Absorption spectra of FAPbBr<sub>3</sub> QDs and their respective negative second derivative, showing the evolution of multiple excitonic absorption transitions. **b**, Analogous study for MAPbBr<sub>3</sub> QDs. All spectra are normalized at 3 eV for a better visual guide of the spectral changes.

# Supplementary Files

This is a list of supplementary files associated with this preprint. Click to download.

- [SIVideo4.mov](#)
- [SIVideo3.mov](#)
- [SIVideo1.mov](#)
- [SIVideo5.mov](#)
- [KovalenkoetalSupplementaryTamingthegrowthofperovskiteQDs.pdf](#)
- [Slvideo2.mp4](#)